

# One second interrogation time in a 200 round-trip waveguide atom interferometer

Hyosub Kim,<sup>1,\*</sup>† Katarzyna Krzyzanowska,<sup>1</sup> K. C. Henderson,<sup>1</sup> C. Ryu,<sup>1</sup> Eddy Timmermans,<sup>2</sup> & Malcolm Boshier<sup>1,‡</sup>

<sup>1</sup>MPA-Q, Los Alamos National Laboratory, Los Alamos, NM 87545,

<sup>2</sup>XCP-5, Los Alamos National Laboratory, Los Alamos, NM 87545

(Dated: April 4, 2022)

We report a multiple-loop guided atom interferometer in which the atoms make 200 small-amplitude round-trips, instead of one large single orbit. The approach is enabled by using ultracold <sup>39</sup>K gas and a magnetic Feshbach resonance that can tune the *s*-wave scattering length across zero to significantly reduce the atom loss from cold collisions. This scheme is resilient against noisy environments, achieving 0.9 s interrogation time without any vibration noise isolation or cancellation. A form of quantum lock-in amplification can be used with the device to measure localized potentials with high sensitivity. We used this technique to measure the dynamic polarizability of the <sup>39</sup>K ground state at 1064 nm. The interferometer may also be a useful approach to building a compact multiple-loop Sagnac atom interferometer for rotation sensing.

Light pulse atom interferometers are important measurement tools in areas ranging from fundamental science to practical applications such as inertial sensing [1, 2]. The most widely-used atom interferometer is the free-space Mach-Zehnder configuration in which an atomic wave packet is split by a beamsplitter light pulse into two wavepackets which move apart before being reflected by a mirror light pulse and then subjected to a second beamsplitter pulse when the wavepackets overlap again. Long interrogation times are desirable because sensitivity scales as the square of the interrogation time. However, because the atoms are falling freely under gravity during the interrogation sequence the most sensitive free-space atom interferometers are several meters high [3], which is incompatible with applications requiring a high-performance portable instrument [4].

The guided atom interferometer, a matter wave analogy of the fiber optic interferometer, is a promising path to the goal of a sensitive compact atom interferometer [5–9] because the waveguide supports the atoms against gravity during the interferometer sequence. Since the waveguide potential affects the propagation and phase accumulation of the matter wave packets it is essential that it be stable, flat, and smooth. While painted waveguide structures [10] can be flat and smooth, it has not yet been shown that guide potential fluctuations can be made sufficiently small for atom interferometry. In waveguides formed by laser beams [11] or magnetic fields from macroscopic coils [12] the potential can be smooth and, if the potential is symmetric, fluctuations made common mode so that they do not affect the interferometer phase. Potentials made in this way necessarily have some curvature along the waveguide, an imperfection which can reduce the interferometer contrast over time, limiting the usable interrogation time [7, 13]. The longest interrogation time reported to date for a waveguide atom interferometer appears to be 100 ms [7].

We report a guided atom interferometer exhibiting high contrast fringes with an interrogation time of over one second in a waveguide with significant curvature. Using a non-interacting Bose-Einstein condensate as the matter wave source enables a multiple loop scheme [14–16] involving hundreds of short round trips in the guide because the contrast-

degrading scattering that occurs when the wavepackets pass through each other is suppressed. The fast modulation of wavepacket momentum by the high reflection rate implements a form of dynamic decoupling [17] or phase sensitive detection [18] that greatly reduces the effect of technical phase noise in the interferometer, to the point where the instrument operates in a noisy environment with no vibration isolation or stabilization of the inertial reference mirror. That is a very desirable characteristic for an atom interferometer that is practical to use outside of the laboratory. The interferometer is particularly well-suited to measuring rotation through the Sagnac effect [15, 16] and to probing interesting weak interactions [19, 20] on micron-scale distances.

The experimental scheme is shown in Fig. 1. Full details are provided in the Supplemental Material. The interferometer sequence starts with formation of a nearly pure Bose-Einstein condensate (BEC) of <sup>39</sup>K in the  $|F, m_F\rangle = |1, -1\rangle$  state near the center of a one-dimensional waveguide with trapping frequencies  $\omega_{x,y,z} = 2\pi(77, 100, 2.8)$  Hz. The <sup>39</sup>K isotope is useful because of a convenient Feshbach resonance [21] that allows a magnetic field to tune the *s*-wave scattering length through zero [22, 23] and to control the collisional loss [24]. The waveguide potential is a combination of the approximately harmonic transverse optical dipole potential ( $\omega_x = 2\pi \times 77$  Hz and  $\omega_y = 2\pi \times 100$  Hz) of a 1064 nm laser beam and a harmonic axial magnetic potential ( $\omega_z = 2\pi \times 2.8$  Hz) arising from the residual curvature in the Helmholtz coils that control the interaction strength. An undesirable compression mode of the BEC along the *z*-axis is induced during the condensate preparation [25, 26]. The interferometer beamsplitters and mirrors are formed by pulses of a 766 nm standing wave, aligned with the waveguide, that impart or change the wavepacket momentum by Bragg diffraction [27–29]. As shown in Fig. 1(a) and (b), the first splitting pulse transforms the initially stationary condensate into a coherent superposition of two momentum states,  $(\psi_+ + \psi_-)/\sqrt{2}$ , and the subsequent series of *n* mirror pulses each switch the direction of momentum,  $\psi_+ \leftrightarrow \psi_-$ . The last splitting pulse with adjustable Bragg laser phase  $\theta$  recombines the atoms, and the atom numbers in each momen-

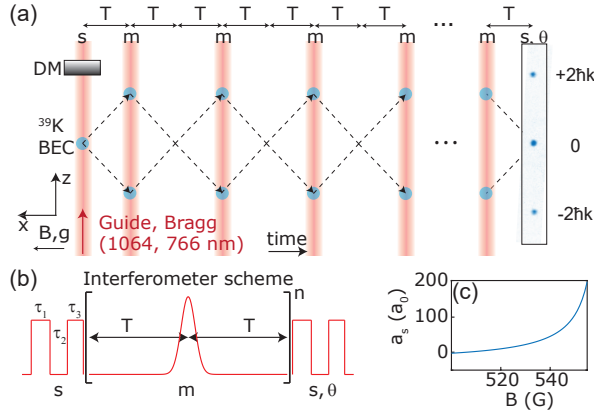


FIG. 1. Experimental scheme. (a) A 1064 nm laser beam creates the guide potential and a collinear 766 nm laser beam (both represented by the wide pink line) creates the optical Bragg grating by retro-reflection from a long-pass dichroic mirror (DM). A  $^{39}\text{K}$   $|F, m_F\rangle = |1, -1\rangle$  BEC (blue circle) is loaded into the waveguide. In the guide, two momentum states  $\pm 2\hbar k$ , with  $k = 2\pi/766$  nm periodically bounce back and forth in response to a series of mirror pulses applied after the splitting. The last beamsplitter pulse recombines the wavepackets with adjustable Bragg laser phase  $\theta$ , and the atom numbers are measured by absorption imaging, as shown at the right-most side. The image is a single shot, showing a  $0.18 \text{ mm} \times 1.47 \text{ mm}$  region after 16 ms of free-expansion without the waveguide. The black arrow labeled  $B, g$  shows the direction of the Helmholtz magnetic field and gravity. (b) The interferometer scheme is composed of a series of regularly-spaced mirror pulses ( $m$ ) sandwiched between the two beam splitter pulses ( $s$ ). The beamsplitter uses square pulses of duration  $\tau_1$  and  $\tau_3$  separated by delay  $\tau_2$  [29], with  $(\tau_1, \tau_2, \tau_3) = (9.7, 16.5, 9.2) \mu\text{s}$  and the reflection pulse is a Gaussian of  $59.8 \mu\text{s}$  FWHM. (c) The magnetic field dependence of the  $s$ -wave scattering length  $a_s$ , in units of Bohr radius  $a_0$ , around the Feshbach resonance used to tune the strength of the interatomic interaction.

tum state  $(N_{+, -, 0})$  are measured by absorption imaging using a fringe suppression algorithm [30, 31]. The interferometer phase is a linear combination of the Bragg pulse phases seen by the atoms that takes the form of a sum with alternating sign,  $\phi_{\text{laser}} = \phi_{\pi/2} + [2 \sum_{i=1}^{n=\text{even}} (-1)^i \phi_{n,\pi}] - \phi_{\pi/2,\theta}$  [32].

Figure 2(a) illustrates some challenges implicit in waveguide atom interferometry. The inset shows both the raw data for a fringe (gray dots, the fraction of atoms in the  $\pm 2\hbar k$  momentum state versus the phase of the final Bragg pulse) and the resulting averaged interference fringe (red diamonds and black line). The envelope of the raw data indicates the underlying fringe contrast  $C_{\text{max}}$ , which is reduced by technical phase noise to the lower value  $C$  given by the amplitude of the averaged fringe. Figure 2(a) shows both measures of contrast for a double loop ( $n = 2$ ) interferometer as a function of half the reflection pulse separation time  $T$ . The contrast decreases with increasing  $T$  for two reasons: the axial curvature in the waveguide potential and the phase noise resulting from mechanical vibrations of the retro-reflecting mirror. The curvature effect is seen in the behavior of  $C_{\text{max}}$  (blue circles), which shows a large reduction in contrast when  $T$  exceeds a

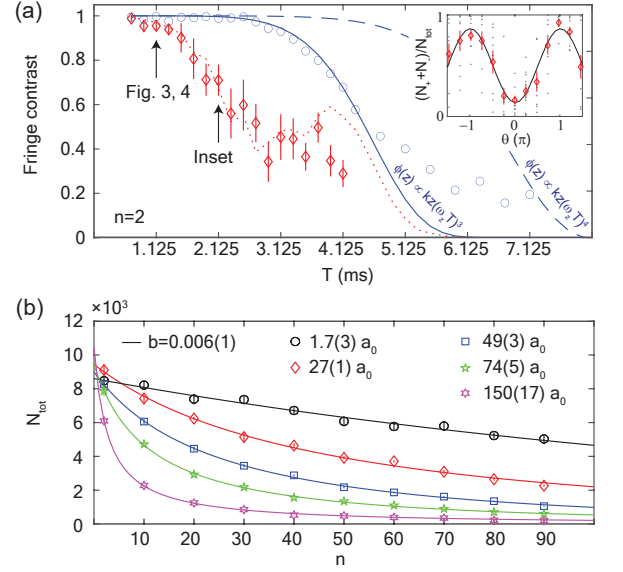


FIG. 2. Analysis of mechanisms limiting interrogation time. (a) The fringe contrast as a function of  $T$  at  $n = 2$  and  $a_s = 1.7a_0$ . Blue circles and red diamonds indicate the maximum possible fringe contrast  $C_{\text{max}}$  and the averaged fringe contrast  $C$ , respectively. Dashed and solid blue lines are the theoretical  $C_{\text{max}}$  taking into account the waveguide curvature and the compressional mode, respectively. The red dotted line is a Monte-Carlo simulation of  $C$  that includes the reference mirror vibration. (Inset) Raw data of atom split ratio. (b) Atom numbers  $N_{\text{tot}}$  as a function of  $n$  for different  $a_s$ . Symbols and lines are averaged data and numerical fits (see text). The mirror pulse efficiency is  $1 - b = 99.4(1)\%$  (black line).  $N_{\text{tot}} = N_+ + N_- + N_0$ . Error bars are the standard error in the mean.

few ms due to the spatial phase gradient over the wave packet (blue lines, see Supplemental Material) [7]. The shot-to-shot phase fluctuations from mechanical noise further reduce the average fringe contrast  $C$  (red diamonds). The behavior is in good agreement with a model based on the measured mechanical motion of the reference mirror (red dotted line, see Supplemental Material).

The main result of this paper is that using many reflections with short  $T$  to confine the atoms near in the center of the guide, rather than a few large amplitude excursions in which the atoms would see more curvature, mitigates the reductions in contrast due to curvature [7] and to vibration-induced phase noise. A potential concern with this approach is that in general the two wavepackets will lose atoms due to scattering every time they pass through each other. This process is illustrated in Fig. 2(b), where the total atom number  $N_{\text{tot}}$  is plotted as a function of the number of reflections  $n$  for various  $a_s$ . The fitted curves are the analytic solution of the differential equation  $dN_{\text{tot}}/dn = -aN_{\text{tot}}^2 - bN_{\text{tot}}$  describing one- and two-body loss. We can associate the coefficient  $b$  with the loss rate of a mirror pulse because the exponential decay time of stationary atom numbers is longer than 20 s for  $a_s < 200 a_0$ . The current mirror efficiency  $99.4(1)\%$  can sustain up to  $n = 400$  loops if the two-body loss rate is sufficiently small. We find that the coefficient  $a$  scales like  $a_s^2$ , in agreement with theory

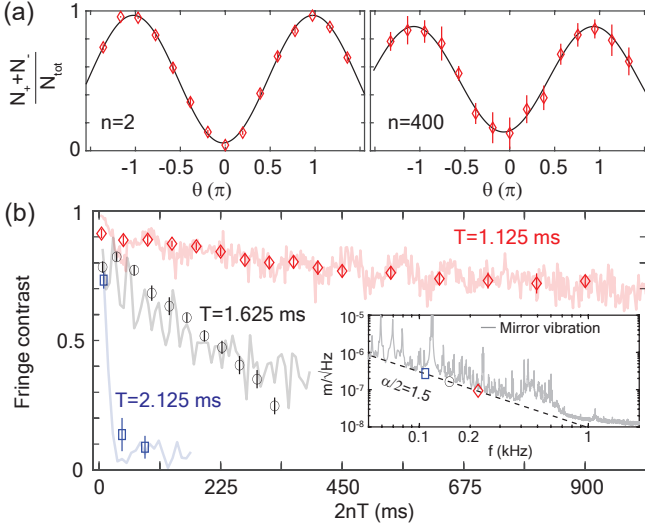


FIG. 3. Results of the multiple-loop atom interferometer. (a) Split ratio  $(N_+ + N_-)/N_{tot}$  as a function of final beamsplitter phase  $\theta$  for  $T = 1.125$  ms and  $a_s = 1.7a_0$ . Red symbols are the averages of at least 8 shots. Black lines are fits to the function  $[1 - C \cos(\theta + \phi)]/2$ , where  $C = 0.91(2), 0.73(3)$  and  $\phi = 0.07(2), 0.21(3)$  radians are respectively the fringe contrast and interferometer phase. (b) Fringe contrast as a function of  $n$  for different  $T$  at  $a_s = 1.7a_0$ . Symbols indicate the average fringe contrast. Faint solid lines are the results of a Monte-Carlo simulation (see Supplemental Material). Inset: The noise amplitude spectrum of the reference mirror on a log-log scale. The dashed lines are the noise slope. Error bars are the standard error in the mean.

(see Fig. 10) [24]. The fitted curve at  $a_s = 1.7 a_0$  is indistinguishable from the case of coefficient  $a = 0$  (see Table I), showing that the collisional loss can effectively be eliminated by magnetic field control of  $a_s$ . We used  $a_s = 1.7a_0$  for the rest of the experiments.

Figure 3(a) compares interferometer fringes corresponding to  $n = 2$  reflections (one round-trip) and to  $n = 400$  reflections (200 round-trips) for  $T = 1.125$  ms under this condition of negligible scattering loss. We chose  $n$  to be even because the resulting symmetrical interferometer suppresses effects that would reduce fringe contrast (see Fig. 8) [7]. We have observed fringes with contrast  $C = 0.73(3)$  after an interrogation time  $2nT = 900$  ms (Fig. 3(b)), which is an order of magnitude longer than previous waveguide atom interferometers [7–9]. Moreover, the practical total interrogation time is currently limited by atom loss from the interferometer due to the slightly imperfect mirror reflectivity (black curve in Fig. 2(b)) because the interaction-induced dephasing is much slower than the measured interrogation times for small  $a_s$  [22, 33]. A number of round trips  $n = 2,000$  (expected interrogation time 4.5 s) should be possible if the reflection pulse efficiency is improved to 99.9% by reducing the momentum width of the atoms [27]. That will be possible if the amplitude of the compressional mode is reduced by employing an appropriate loading sequence of the BEC [25]. It is useful to compare our approach to that of Ref. [34] in which

a bright soliton ( $a_s < 0$ ) was used to compensate for the wave packet dispersion. Here we can choose a positive  $a_s$  because of the compressional mode, which will allow the atom number, and hence the signal, to be larger than is possible for the soliton approach.

It is remarkable that the long interrogation time is obtained without any mechanical noise cancellation or isolation—the optical table supporting the atom interferometer sits on rigid legs standing on the laboratory floor. This noise immunity arises because the form of the interferometer phase as an alternating sign sum of phases leads to an interferometer response to Bragg pulse phase noise which acts as a pass band filter of frequency  $1/(4T)$ , similar to lock-in detection [18], suggesting that the system might be useful for noise spectrum analysis [35]. Figure 3(b) shows that the multiple-loop configuration with short  $T$  improves the available interrogation time by at least two orders of magnitude. The faint bands show the predictions of a model in which the phase of the atom-laser interaction was calculated classically as if the wave packet was a point particle (see Supplemental Material) [32]. It is in good agreement with the experimental data. We observed that the fringe contrast at fixed  $n$  dropped rapidly with increasing  $T$  [Fig. 3(b)]. We found that the phase noise scales as  $\delta\phi_{laser}^2 \propto 2n(2T)^\alpha$  for  $n \gg 1$  (see Fig. 7), and the noise slope  $\alpha$  at the region is steep enough to wash out the fringe (see inset of Fig. 3(b)). This result shows that the multiple-loop scheme outperforms the single loop approach in an environment where the noise power spectral density scales like  $1/f^\alpha$  when  $\alpha > 1$ .

We have used the lock-in like response of the multiple-loop atom interferometer to measure the AC Stark shift [36] produced by a 1064 nm Gaussian beam of waist  $w_0 = 85(1) \mu\text{m}$  and maximum intensity  $I_0$  overlapping the waveguide and propagating perpendicular to it (Fig. 4). This application highlights another advantage of the multiple-loop approach for measuring localized interactions, namely that the atoms can accumulate phase shifts from the interaction many times during the total interrogation time, thereby boosting the sensitivity. The on/off state of the AC Stark shift beam is switched every time the wavepackets cross in the center of the waveguide (inset of Fig. 4(b)). This synchronous signal modulation results in the highest sensitivity as the interferometer coherently accumulates the extra phase shift from the interaction (see also Fig. 11). The red line in Fig. 4(b) is a least-squares fit of the data to the expected AC Stark shift,  $U(z, t) = \alpha_{1064 nm} I(t) \exp(-2z^2/w_0^2)/(2\epsilon_0 c)$ . From this fit we find a value for the ground state polarizability of  $\alpha_{1064 nm} = 620(40)$  atomic units, which is in good agreement with the reference value  $599.14(47)$  atomic units [37]. The multiple-loop phase-sensitive atom interferometer would be ideal for measuring interactions of the wavepackets with a localized source in which the size is comparable to or smaller than the atom separation, since the phase could accumulate coherently as the wavepackets make multiple trips past the source, becoming  $n$  times the single-loop phase shift after  $n$

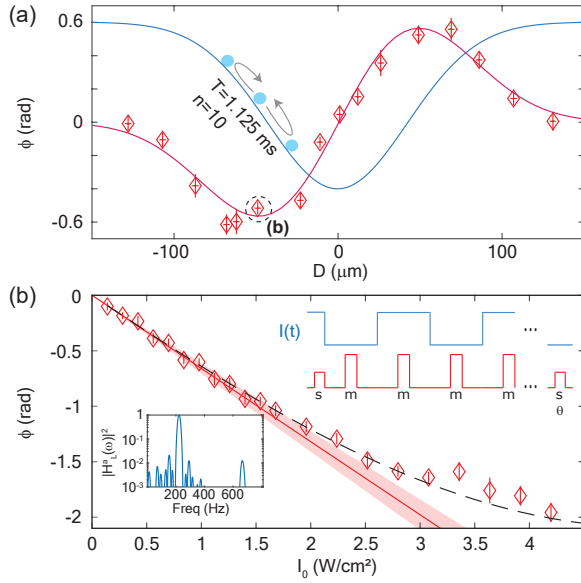


FIG. 4. Measurement of a high spatial gradient signal via lock-in detection. (a) Red diamonds and line are the measured and calculated interferometer phase shift respectively as a function of the distance  $D$  between the center of the beam creating the AC Stark shift and the initial position of the BEC. The blue line is the 1064 nm beam profile of waist  $(1/e^2)$   $85(1) \mu\text{m}$ . (b) Red diamonds are the phases as a function of the peak intensity. Red line and its area are the theory without a free parameter and 7% uncertainty of power and size measurement, respectively. Inset: The transfer function of acceleration is a band-pass filter that is sensitive to the 1064 nm intensity modulation,  $I(t) = I_0[1 + \text{sign}\{\sin(2\pi Ft)\}]/2$ , where  $F = 1/(4T)$ . It happened that  $I(t < 0) = I_0$  pulls the atoms to the beam center and causes the loss of the linearity (black dashed line). Error bars are the standard error in the mean.

round trips.

In addition to the possibility of phase-sensitive detection, the multiple-loop approach might offer better signal-to-noise ratio than that of a single loop in situations where mechanical vibrations transmitted to the retro-reflecting mirror create significant phase noise. An important application of the multiple-loop scheme is the case of a Sagnac atom interferometer realized by moving the waveguide in a horizontal plane transversely back and forth synchronous with the reflection pulse sequence so that the wavepacket trajectories enclose area [38] or by using a closed loop waveguide [10, 39, 40]. The enclosed area and hence the Sagnac phase is proportional to the number of loops, amplifying the signal without increasing the physical size of the interferometer.

Looking to the future, we believe that  $T = 20$  ms is feasible for a moderate waveguide beam waist ( $100 \mu\text{m}$ ) with active vibration reduction and removal of waveguide curvature  $\omega_z$ . It will be possible to reduce  $\omega_z$  by optimizing the magnetic coil geometry and reducing the field to 100 G to exploit another Feshbach resonance where  $a_s = 7a_0$  and  $dE/dB = 34 \text{ kHz/G}$  for  $^{39}\text{K}$   $|F, m_F\rangle = |1, -1\rangle$  [21]. Strontium atoms are also a good choice for atom interferometry

since they have small  $a_s$  and zero magnetic moment [6]. If the mirror pulse efficiency is optimized to 99.9%, an interrogation time of 60 s should be possible.

We have demonstrated multiple-loop atom interferometry in a waveguide. Collisional loss is suppressed deploying a magnetic Feshbach resonance, reducing the  $s$ -wave scattering length close to zero. The interrogation times are extended by two orders of magnitude from the single-loop limit set by the waveguide curvature and technical noise. We have also demonstrated quantum lock-in amplification [18]. The system may be useful for multiple-loop Sagnac interferometry [15], for noise spectrum analysis [35] and, perhaps, for resonant detection of gravitational waves [41].

## ACKNOWLEDGMENTS

We would like to acknowledge Saurabh Pandey for useful comments, Doga Kurkcuoglu for theoretical help, Nick Dallmann for the loan of a network analyzer, and Carlo Samson for work on the design and construction of the apparatus. This work was supported by the U.S. Department of Energy through awards 20180045DR and 20180753PRD3 of the LANL Laboratory Directed Research and Development program.

\*E-mail: khs89p@gmail.com

‡E-mail: boshier@lanl.gov

†Current address: Atom Computing, Inc., Boulder, Colorado 80301, USA

- [1] K. Bongs, M. Holynski, J. Vovrosh, P. Bouyer, G. Condon, E. Rasel, C. Schubert, W. P. Schleich, and A. Roura, Taking atom interferometric quantum sensors from the laboratory to real-world applications, *Nature Reviews Physics* **1**, 731 (2019).
- [2] A. D. Cronin, J. Schmiedmayer, and D. E. Pritchard, Optics and interferometry with atoms and molecules, *Reviews of Modern Physics* **81**, 1051 (2009).
- [3] P. Asenbaum, C. Overstreet, T. Kovachy, D. D. Brown, J. M. Hogan, and M. A. Kasevich, Phase shift in an atom interferometer due to spacetime curvature across its wave function, *Physical Review Letters* **118**, 183602 (2017).
- [4] X. Wu, Z. Pagel, B. S. Malek, T. H. Nguyen, F. Zi, D. S. Scheirer, and H. Müller, Gravity surveys using a mobile atom interferometer, *Science Advances* **5**, eaax0800 (2019).
- [5] V. Xu, M. Jaffe, C. D. Panda, S. L. Kristensen, L. W. Clark, and H. Müller, Probing gravity by holding atoms for 20 seconds, *Science* **366**, 745 (2019).
- [6] X. Zhang, R. P. del Aguila, T. Mazzoni, N. Poli, and G. M. Tino, Trapped-atom interferometer with ultracold Sr atoms, *Physical Review A* **94**, 043608 (2016).
- [7] J. H. T. Burke, B. Deissler, K. J. Hughes, and C. A. Sackett, Confinement effects in a guided-wave atom interferometer with millimeter-scale arm separation, *Physical Review A* **78**, 023619 (2008).



- [8] G. B. Jo, Y. Shin, S. Will, T. A. Pasquini, M. Saba, W. Ketterle, D. E. Pritchard, M. Vengalattore, and M. Prentiss, Long phase coherence time and number squeezing of two Bose-Einstein condensates on an atom chip, *Physical Review Letters* **98**, 030407 (2007).
- [9] Y.-J. Wang, D. Z. Anderson, V. M. Bright, E. A. Cornell, Q. Diot, T. Kishimoto, M. Prentiss, R. A. Saravanan, S. R. Segal, and S. Wu, Atom Michelson interferometer on a chip using a Bose-Einstein condensate, *Physical Review Letters* **94**, 090405 (2005).
- [10] C. Ryu and M. G. Boshier, Integrated coherent matter wave circuits, *New Journal of Physics* **17**, 092002 (2015).
- [11] G. D. McDonald, H. Keal, P. A. Altin, J. E. Debs, S. Bennetts, C. C. N. Kuhn, K. S. Hardman, M. T. Johnsson, J. D. Close, and N. P. Robins, Optically guided linear Mach-Zehnder atom interferometer, *Physical Review A* **87**, 013632 (2013).
- [12] O. Garcia, B. Deissler, K. J. Hughes, J. M. Reeves, and C. A. Sackett, Bose-Einstein-condensate interferometer with macroscopic arm separation, *Physical Review A* **74**, 031601 (2006).
- [13] R. H. Leonard and C. A. Sackett, Effect of trap anharmonicity on a free-oscillation atom interferometer, *Physical Review A* **86**, 043613 (2012).
- [14] J. M. McGuirk, G. T. Foster, J. B. Fixler, M. J. Snadden, and M. A. Kasevich, Sensitive absolute-gravity gradiometry using atom interferometry, *Physical Review A* **65**, 033608 (2002).
- [15] C. Schubert, S. Abend, M. Gersemann, M. Gebbe, D. Schlippert, P. Berg, and E. M. Rasel, Multi-loop atomic Sagnac interferometry, *Scientific Reports* **11**, 16121 (2021).
- [16] L. A. Sidorenkov, R. Gautier, M. Altorio, R. Geiger, and A. Landragin, Tailoring multiloop atom interferometers with adjustable momentum transfer, *Physical Review Letters* **125**, 213201 (2020).
- [17] E. L. Hahn, Spin echoes, *Physical Review* **80**, 580 (1950).
- [18] S. Kotler, N. Akerman, Y. Glickman, A. Keselman, and R. Ozeri, Single-ion quantum lock-in amplifier, *Nature* **473**, 61 (2011).
- [19] M. Jaffe, P. Haslinger, V. Xu, P. Hamilton, A. Upadhye, B. Elder, J. Khoury, and H. Müller, Testing sub-gravitational forces on atoms from a miniature in-vacuum source mass, *Nature Physics* **13**, 938 (2017).
- [20] P. Haslinger, M. Jaffe, V. Xu, O. Schwartz, M. Sonnleitner, M. Ritsch-Marte, H. Ritsch, and H. Müller, Attractive force on atoms due to blackbody radiation, *Nature Physics* **14**, 257 (2018).
- [21] C. D’Errico, M. Zaccanti, M. Fattori, G. Roati, M. Inguscio, G. Modugno, and A. Simoni, Feshbach resonances in ultracold  $^{39}\text{K}$ , *New Journal of Physics* **9**, 223 (2007).
- [22] M. Fattori, C. D’Errico, G. Roati, M. Zaccanti, M. Jonas-Lasinio, M. Modugno, M. Inguscio, and G. Modugno, Atom interferometry with a weakly interacting Bose-Einstein condensate, *Physical Review Letters* **100**, 080405 (2008).
- [23] G. Roati, M. Zaccanti, C. D’Errico, J. Catani, M. Modugno, A. Simoni, M. Inguscio, and G. Modugno,  $^{39}\text{K}$  Bose-Einstein condensate with tunable interactions, *Physical Review Letters* **99**, 010403 (2007).
- [24] Y. B. Band, M. Trippenbach, J. P. Burke, and P. S. Julienne, Elastic scattering loss of atoms from colliding Bose-Einstein condensate wave packets, *Physical Review Letters* **84**, 5462 (2000).
- [25] A. Di Carli, C. D. Colquhoun, G. Henderson, S. Flannigan, G.-L. Oppo, A. J. Daley, S. Kuhr, and E. Haller, Excitation modes of bright matter-wave solitons, *Physical Review Letters* **123**, 123602 (2019).
- [26] E. Haller, M. Gustavsson, M. J. Mark, J. G. Danzl, R. Hart, G. Pupillo, and H.-C. Nägerl, Realization of an excited, strongly correlated quantum gas phase, *Science* **325**, 1224 (2009).
- [27] S. S. Szigeti, J. E. Debs, J. J. Hope, N. P. Robins, and J. D. Close, Why momentum width matters for atom interferometry with Bragg pulses, *New Journal of Physics* **14**, 023009 (2012).
- [28] H. Müller, S.-w. Chiow, and S. Chu, Atom-wave diffraction between the raman-nath and the Bragg regime: Effective Rabi frequency, losses, and phase shifts, *Physical Review A* **77**, 023609 (2008).
- [29] S. Wu, Y.-J. Wang, Q. Diot, and M. Prentiss, Splitting matter waves using an optimized standing-wave light-pulse sequence, *Physical Review A* **71**, 043602 (2005).
- [30] L. Niu, X. Guo, Y. Zhan, X. Chen, W. M. Liu, and X. Zhou, Optimized fringe removal algorithm for absorption images, *Applied Physics Letters* **113**, 144103 (2018).
- [31] C. F. Ockeloen, A. F. Tauschinsky, R. J. C. Spreeuw, and S. Whitlock, Detection of small atom numbers through image processing, *Physical Review A* **82**, 061606 (2010).
- [32] A. Peters, K. Y. Chung, and S. Chu, High-precision gravity measurements using atom interferometry, *Metrologia* **38**, 25 (2001).
- [33] M. Gustavsson, E. Haller, M. J. Mark, J. G. Danzl, G. Rojas-Kopeinig, and H. C. Nägerl, Control of interaction-induced dephasing of Bloch oscillations, *Physical Review Letters* **100**, 080404 (2008).
- [34] G. D. McDonald, C. C. N. Kuhn, K. S. Hardman, S. Bennetts, P. J. Everitt, P. A. Altin, J. E. Debs, J. D. Close, and N. P. Robins, Bright solitonic matter-wave interferometer, *Physical Review Letters* **113**, 013002 (2014).
- [35] T. Yuge, S. Sasaki, and Y. Hirayama, Measurement of the noise spectrum using a multiple-pulse sequence, *Physical Review Letters* **107**, 170504 (2011).
- [36] B. Deissler, K. J. Hughes, J. H. T. Burke, and C. A. Sackett, Measurement of the ac Stark shift with a guided matter-wave interferometer, *Physical Review A* **77**, 031604 (2008).
- [37] B. Parinaz, M. Adam, A. Bindiya, E. Rudolf, and S. S. Marianna, *Portal for high-precision atomic data and computation (version 1.0)* (2021).
- [38] K. Krzyzanowska, J. Ferreras, C. Ryu, C. Samson, and M. Boshier, Matter wave analog of a fiber optic gyro, in preparation (2022).
- [39] S. Pandey, H. Mas, G. Drougakis, P. Thekkeppatt, V. Bolpasi, G. Vasilakis, K. Poullos, and W. von Klitzing, Hyper-sonic Bose-Einstein condensates in accelerator rings, *Nature* **570**, 205 (2019).
- [40] E. R. Moan, R. A. Horne, T. Arpornthip, Z. Luo, A. J. Fallon, S. J. Berl, and C. A. Sackett, Quantum rotation sensing with dual Sagnac interferometers in an atom-optical waveguide, *Physical Review Letters* **124**, 120403 (2020).
- [41] P. W. Graham, J. M. Hogan, M. A. Kasevich, and S. Rajendran, Resonant mode for gravitational wave detectors based on atom interferometry, *Physical Review D* **94**, 104022 (2016).
- [42] M. Landini, S. Roy, G. Roati, A. Simoni, M. Inguscio, G. Modugno, and M. Fattori, Direct evaporative cooling of  $^{39}\text{K}$  atoms to Bose-Einstein condensation, *Physical Review A* **86**, 033421 (2012).
- [43] G. Salomon, L. Fouché, P. Wang, A. Aspect, P. Bouyer, and T. Bourdel, Gray-molasses cooling of  $^{39}\text{K}$  to a high phase-space density, *EPL (Europhysics Letters)* **104**, 63002 (2013).
- [44] A. Couvert, T. Kawalec, G. Reinaudi, and D. Guéry-Odelin, Optimal transport of ultracold atoms in the non-adiabatic regime, *EPL (Europhysics Letters)* **83**, 13001 (2008).

- [45] C. Gross, H. C. J. Gan, and K. Dieckmann, All-optical production and transport of a large  $^6\text{Li}$  quantum gas in a crossed optical dipole trap, [Physical Review A \*\*93\*\*, 053424 \(2016\)](#).
- [46] D. M. Stamper-Kurn, H. J. Miesner, A. P. Chikkatur, S. Inouye, J. Stenger, and W. Ketterle, Reversible formation of a Bose-Einstein condensate, [Physical Review Letters \*\*81\*\*, 2194 \(1998\)](#).
- [47] P. W. H. Pinkse, A. Mosk, M. Weidemüller, M. W. Reynolds, T. W. Hijmans, and J. T. M. Walraven, Adiabatically changing the phase-space density of a trapped Bose gas, [Physical Review Letters \*\*78\*\*, 990 \(1997\)](#).
- [48] K. M. O'Hara, M. E. Gehm, S. R. Granade, and J. E. Thomas, Scaling laws for evaporative cooling in time-dependent optical traps, [Physical Review A \*\*64\*\*, 051403 \(2001\)](#).
- [49] M. S. Crosser, S. Scott, A. Clark, and P. M. Wilt, On the magnetic field near the center of Helmholtz coils, [Review of Scientific Instruments \*\*81\*\*, 084701 \(2010\)](#).

## SUPPLEMENTAL MATERIAL

### BEC preparation

Preparation of nearly pure BEC for the experiment discussed in this paper is achieved in three stages. As shown in Fig. 5, the apparatus consists of two vacuum chambers plus a glass cell where the BEC is prepared. The first stage takes place in a relatively high pressure chamber where  $^{39}\text{K}$  cold atoms are continuously loaded into a 3D  $D2$ -line magneto-optical trap (MOT) from a vapor provided by commercial getter sources. This high pressure chamber is separated from the rest of the system by a constriction and an empty chamber with an ion pump, enabling differential pumping. Simultaneously, a near-resonance push beam ( $D2$  cooling plus repumping light) overlapped with the high pressure MOT continuously pushes atoms towards the second MOT in the low pressure chamber. Atoms are collected in the low pressure MOT for about 5 s, with a loading rate  $\sim 10^8$  atoms/s.

Once the atomic cloud is formed in the low pressure chamber, the push beam is blocked and the second stage of the preparation begins. It starts with 50 ms  $D2$  compression with field gradient 24 G/cm [42], followed by 10 ms of  $D1$ - $D2$  hybrid compression. At this stage the peak density of the atomic cloud is  $\sim 8 \times 10^{10}$  atoms/cm $^3$  with 60  $\mu\text{K}$  temperature. Next, the temperature is reduced to 6  $\mu\text{K}$  using  $D1$  gray molasses technique with the magnetic field gradient set to near zero for 7 ms [43]. The atoms are optically pumped into the  $F = 1$  manifold by turning off the  $D1$  repump light for the last 3 ms of gray molasses. The resulting atoms are then captured in a magnetic trap by turning on the MOT anti-Helmholtz coils at a gradient of 44 G/cm which is then ramped linearly to 200 G/cm over 100 ms. Confinement in a tight magnetic trap provides the time needed to overlap a dipole trap beam with the atomic cloud for about 2 s and load a sufficiently high fraction of atoms into the beam.

The dipole trap beam is a 1550 nm single mode laser (IPG photonics, ELR-LP-SF-30) with a total power 20 W and active power stabilization. The beam is focused by a singlet lens with  $f = 750$  mm and delivered to the low pressure chamber, providing 720  $\mu\text{K}$  trap depth and  $2\pi \times 36$  Hz axial trap

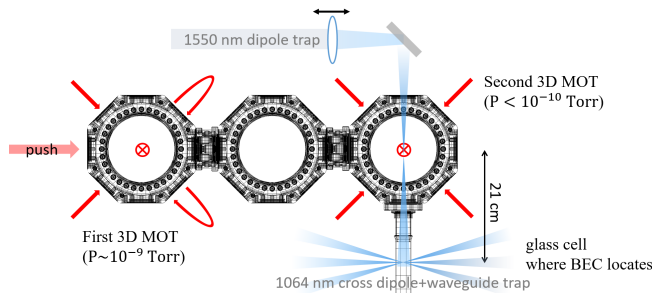


FIG. 5. Experimental setup of three-stage BEC machine.

frequency. Importantly, the dipole trap is slightly displaced from the center of the magnetic trap to hold the spin polarized atoms. Once the dipole trap is loaded from the magnetic trap, the magnetic field is turned off. A typical atom number density and temperature in the dipole trap obtained at this point are  $\sim 10^6$ ,  $10^{11}\text{cm}^{-3}$  and 15  $\mu\text{K}$  respectively.

In the final stage of the preparation, the atoms are transferred to the science cell by translating the lens on a linear motor stage (Newport, XML350) at a distance 215 mm during a 900 ms trajectory [44, 45]. The velocity profile of the translation stage has isosceles trapezoid shape of maximum velocity 280 mm/s and acceleration 2200 mm/s $^2$ . The transfer efficiency is close to 100% without any discernable heating. The transfer time had to be increased to a few seconds recently because wear in the stage after a million transport cycles increased vibration during transport. The Earth's magnetic field maintains the spin polarization during the transfer. Light-assisted inelastic loss is negligible during the transfer because the trap depth is near the Ramsauer minimum [42].

The transition from thermal cloud to a BEC takes place in the science cell. An additional set of 1064 nm beams is overlapped with the atomic cloud held in 1550 nm dipole trap, as shown in Fig. 5. The s-wave scattering length is set to  $200a_0$  by the magnetic Feshbach resonance at 562 G [21], and the power of the 1550 nm dipole trap is reduced for 1.3s to load the atoms into the 1064 nm cross-dipole trap by the dimple effect [46, 47]. For the next 200 ms an adiabatic compression is applied in the 1064 nm beams by increasing the power by factor of 2 and setting the s-wave scattering length to near zero. Finally, a 5 s step of forced evaporative cooling takes place, when the scattering length is set to  $\sim 500a_0$  and the beams' intensity is ramped [48] to a final trap frequency  $\omega_{x,y,z} = 2\pi(77, 100, 12)$  Hz.

Next, as shown in Fig. 5, the outer two 1064 nm beams in the crossed dipole trap are slowly turned off, transferring the BEC with minimal excitation to the middle ( $z$ -axis in Fig. 1) 1064 nm trapping beam which forms the waveguide. The  $z$ -axis harmonic potential ( $\omega_z = 2\pi \times 2.8$  Hz) is almost entirely due to the inhomogeneity of the field produced by the Helmholtz coils [49]; the  $2\pi \times 0.3$  Hz axial trapping frequency of the guide is negligible. The mismatch in waveguide and trapping potentials excites both center-of-mass motion and a compressional mode (discussed below), but importantly the wavepacket does not disperse during the interferometer interrogation time. Finally, the s-wave scattering length is then set to a desired value by linearly sweeping the magnetic field for 300 ms. The typical BEC preparation time to this point is about 20 s.

### Interferometer sequence

The momentum state of the BEC is manipulated using Bragg scattering from a standing wave of light formed by a 766.5 nm external cavity diode laser detuned 100 GHz blue of the  $D2$  line and delivered to the interaction region with

a polarization-maintaining optical fiber and switched with an acousto-optic modulator. The standing wave is created by retro-reflection from a dichroic mirror (Fig. 1(a)) of a beam with waist  $(1/e^2)$  at the atoms of  $80\text{ }\mu\text{m}$  to prevent interference from overlap of internal reflections from the surfaces of the uncoated glass cell. Sub-ms pulses of the standing wave grating impart  $\pm 2\hbar k$  momentum kicks, where  $k$  is the wave-vector of the Bragg laser [27–29]. As shown in Fig. 1(a), a double square pulse [29] acts as a beamsplitter that transforms the initially stationary atoms into a coherent superposition of two momentum states,  $(\psi_+ + \psi_-)/\sqrt{2}$ . Subsequent gaussian pulses [28] act as mirrors, reversing the momentum of the wavepackets,  $\psi_+ \leftrightarrow \psi_-$ . At the end of the cycle a second beamsplitter pulse with adjustable laser phase  $\theta$  relative to the previous pulses recombines the atoms into a superposition of the two output ports of the interferometer. The waveguide and the magnetic field are then turned off, and the atom numbers in each of the momentum states ( $N_{+,-,0}$ ) are measured by absorption imaging after 16 ms of free expansion. Background noise in the absorption images is reduced with a fringe suppression algorithm [30, 31]. We note that the low spontaneous scattering rate of photons from the Bragg laser ( $2\pi \times 0.03\text{ Hz}$ ) means that process has negligible effect on the interferometer.

The relative phase of the recombination pulse  $\theta$  is tuned by changing the frequency of Bragg laser ( $\delta f$ ) using its built-in piezo-electric tuning element. The resulting phase shift is  $\theta = 8\pi \times \delta f \times d/c$ , where  $d$  is the distance from the mirror to the atoms and  $c$  is the speed of light. In our system where  $d \sim 0.4\text{ m}$ , a frequency shift  $\delta f \sim 100\text{ MHz}$  is enough to change  $\theta$  by  $\pi$ . The intensity and frequency of the Bragg laser are not actively stabilized. Nor are the position and tilt of the retro-reflector.

### BEC dynamics during the interferometer sequence

The transfer of the BEC from the crossed-dipole trap to the waveguide beam is designed to be adiabatic. However, imperfections in the system induce a center-of-mass oscillation and excite a compressional mode of the BEC. The resulting dynamics are shown in Fig. 6, where the center-of-mass position

(left) and the axial width (right) of BEC are plotted as a function of the hold time in the waveguide. The compressional mode frequency  $\omega_c$  and the axial trap frequency  $\omega_z = 2\pi \times [2.8(1), 2.8(1), 2.9(2)]\text{ Hz}$  are found from sinusoidal fits for scattering lengths  $a_s = [-2.5, 0.7, 150]a_0$  respectively. The axial trap frequency of the guide ( $2\pi \times 0.3\text{ Hz}$ ) is negligible; it is the z-axis harmonic potential ( $\omega_z = 2\pi \times 2.8\text{ Hz}$ ) from the inhomogeneity of the Helmholtz coils [49] which induces the compressional mode [25, 26].

The initial center-of-mass momentum can be estimated as  $p_{\text{initial}} = m\omega_z z_{\text{initial}}$ , where  $z_{\text{initial}}$  is the amplitude of the sinusoidal fit. The initial momentum depends on the details of the final steps in the preparation sequence, namely the end of the evaporation and the loading into the waveguide. The center-of-mass position changes as a function of the final s-wave scattering length because the potential minimum moves when the magnetic trap depth is reduced. Since the the BEC is located near the waveguide beam waist, by comparing the minimum position of the combined potential  $m(\omega_z z)^2/2 + mgz\theta_{\text{tilt}}$  to the measured center-of-mass position for various  $\omega_z$ , we can estimate that the tilt angle between the normal of the waveguide and the gravity direction is  $\sim 5\text{ mrad}$ .

The implications for the interferometer sequence are as follows. The estimated tilt, which is ( $\theta_{\text{tilt}} \ll 1$ ), does not affect the phase of the atom interferometer for  $n = \text{even}$  as long as the magnetic field is static. The excursion of each wavepacket ( $\pm 30\text{ }\mu\text{m}$  at  $T = 1.125\text{ ms}$ ) is longer than the wavepacket size  $\sigma_z = 6 \sim 20\text{ }\mu\text{m}$  determined by a Gaussian density fit  $|\psi|^2 \propto \exp(-z^2/2\sigma_z^2)$  (The wavepacket size is time-dependent due to the compressional mode). Therefore the wave packets are well-separated from each other during the interferometer cycle. Finally, the ratio  $\omega_c/\omega_z = [2.1(2), 1.8(1), 1.7(2)]$  for the three scattering lengths shows that our system lies between the non-interacting and 1D Thomas-Fermi regimes [25, 26].

### Phase noise due to retro-reflecting mirror vibration

The interferometer phase ( $\phi_{\text{laser}}$ ) and the phase fluctuation due to technical noise ( $\delta\phi_{\text{laser}}^i$ ) in shot  $i$  are given by

$$\begin{aligned}\phi_{\text{laser}} &= 4kz(0) + 8k \sum_{j=1}^{j=n} (-1)^j z(t_j) + 4k(-1)^{n+1} [z(t_{n+1}) + \frac{\theta}{4k}], \\ \delta\phi_{\text{laser}}^i &= 4k\delta z^i(0) + 8k \sum_{j=1}^{j=n} (-1)^j \delta z^i(t_j) + 4k(-1)^{n+1} \delta z^i(t_{n+1}),\end{aligned}\tag{1}$$

where  $z(t_j)$  and  $\delta z^i(t_j)$  are respectively the center-of-mass position of the atoms and the displacement of the reference mirror when the  $j$ -th pulse hits. Note that the 0-th and  $n+1$ -th pulses are splitting pulses. To find  $z(t_j)$ , we used a 4-th

order Runge-Kutta method to numerically calculate the trajectory of the atoms using  $F = ma$  including the known guide potential and assuming that the photon momentum transfer is instantaneous. To obtain  $\delta z^i(t_j)$ , we independently measured



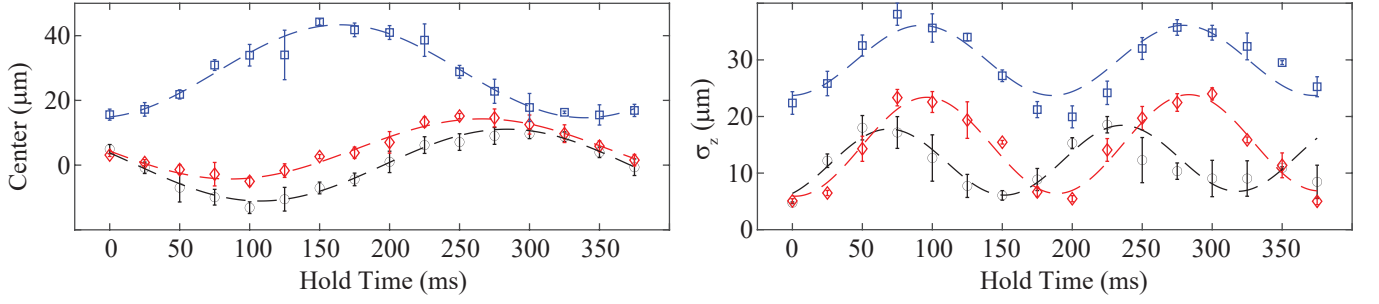


FIG. 6. Center position (left) and axial width  $\sigma_z$  (right) of BEC after 16 ms free expansion, as a function of time in the waveguide. Dashed lines are sinusoidal fits. Error bars are standard error in the mean of at least 4 measurements. (Black circles, red diamonds, blue squares) correspond respectively to the  $s$ -wave scattering length values  $a_s = (-2.5, 0.7, 150)a_0$

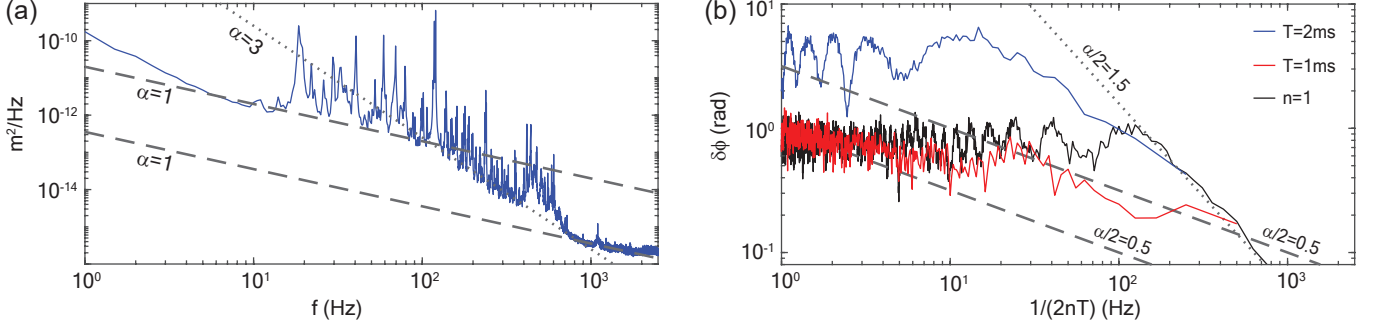


FIG. 7. The mirror position noise spectrum and the corresponding phase noise. (a) The blue line is the reference mirror position noise spectrum density, measured by the independent optical Michelson interferometer. (b) Color lines are the phase fluctuation  $\delta\phi_{laser} = \sqrt{\sum_i \delta\phi_{laser}^{i,2}}$  in Eq. (2). Gray dashed and dotted lines are the noise slope guide.

the reference mirror vibration with an optical Michelson interferometer. The resulting noise amplitude spectrum is shown in the inset of Fig. 3(b) with a fit to the function  $1/f^{\alpha/2}$ . For the numerical estimation of the shot-to-shot phase noise  $\phi_{laser}^i$ ,  $\delta z^i(0)$  is randomly sampled from the time series of the Michelson interferometer data.

### Noise spectrum and phase noise

The main source of reference mirror vibration is the movement of cooling water inside the magnetic field coils. Note that the mirror vibration measured by the optical Michelson interferometer is re-scaled by 0.38 to fit the experimental data in Fig. 3(b). In this section, we focus on the reference mirror vibration-induced phase noise and its relation to the noise spectrum. From Eq. (1), the average laser phase fluctuation becomes

$$\delta\phi_{laser}^2 \propto \overline{\delta z^i(t_{n+1})^2} + 2 \sum_{j=1}^{j=n} \overline{\delta z^i(t_j)^2}, \quad (2)$$

when  $\delta z^i(t)$  is assumed to be a random walk-type fluctuation. Note that  $\delta z^i(0) \equiv 0$  because the displacement at the start of the cycle is taken to be zero. If  $\delta z(t)^2$  is Markovian noise with

spectrum  $1/f^\alpha$ , the average value  $\overline{\delta z^i(t_j)^2} \propto (t_j - t_{j-1})^\alpha$  can be deduced. In the case of a multiple-loop interferometer with parameters  $n$  and  $T$ , Eq. (2) becomes  $\delta\phi^2 \propto 3(T)^\alpha + 2(n-1)(2T)^\alpha \approx 2n(2T)^\alpha$  for  $n \gg 1$ . The corresponding result for a single-loop interferometer with the same interrogation time is  $\delta\phi^2 \propto 3(nT)^\alpha$ . Consequently in the case  $n \gg 1$  and  $\alpha > 1$  the phase noise of the multiple-loop scheme can be smaller than that of the single-loop scheme, as seen in Fig. 7(b) by comparing the red and black curves.

The phase noise calculated using Eq. (1) applied to the optical interferometer data for  $T = 1$  ms (red curve in Fig. 7(b)) has scaling exponent close to 0.5 around 100 Hz, and it shows good agreement with the scaling of  $\sqrt{n}$  from Eq. (2). The phase noise for  $n = 1$  (black line) has scaling exponent close to 1.5 around 100 Hz, which resembles the slope of the noise density in Fig. 7(a) and agrees with Eq. (2). The phase noise for  $T = 2$  ms (blue line) also has a similar slope, which explains the rapid loss of the contrast in Fig. 3(b).

The signal-to-noise ratio (SNR) scales as  $4k_0 a_{max} (nT)^{2-\alpha/2} / \sqrt{3}$  for a single-loop scheme measuring a constant uniform acceleration  $a_{max}$ , when  $\delta\phi_{laser}^2$  is the dominant noise. The SNR for a multiple-loop scheme measuring a square-modulated acceleration scales as  $2^{(1-\alpha)/2} k_0 a_{max} n^{1/2} T^{2-\alpha/2}$ . Therefore the multiple-loop scheme has better SNR when the slope  $\alpha$  of the phase noise

satisfies  $\alpha > 3$ .

### Numerical simulation of fringe contrast

Equation (1) treats the atoms as classical point-like particles. For a more complete simulation using finite size wave packet, the maximum fringe contrast is  $C_{max} = \int |\psi_+ \psi_-^*| \cos \phi_{laser}(z) dz$ , where  $|\psi_+ \psi_-^*| = |\psi|^2$  and  $\phi_{laser}(z)$  is the axial position dependent phase from Eq. (1). The averaged fringe contrast is  $C = C_{max} \times \overline{\cos \phi_{laser}^i}$ . Note that  $\phi_{laser}(z) = 4kz(\omega_z T)^2$  for  $n = \text{odd}$  and  $\omega_z T \ll 1$ , which is an inhomogeneous dephasing imprinted along the wave packet due to the axial curvature of the potential. Note that if  $n$  is even then the inhomogeneous dephasing terms cancel to zero, leaving the next highest order contribution as the leading term. Reference [7] has shown analytically that the next order is  $(\omega_z T)^6$ , but our numerical estimation found it to be  $\phi(z) = \phi_{laser} + \phi_{path} \sim 47kz(\omega_z T)^4$ , where  $\phi_{path} = (S_+ - S_-)/\hbar$  is the phase from the classical action [20]; the second order term comes from the energy loss when the atoms climb up the potential while the momentum kicks are always constant.

The blue dashed line in Fig. 3(a) is calculated for  $C_{max} = \int |\psi_+ \psi_-^*| \cos(\phi(z)) dz$ , where  $\psi_{\pm} = \exp[-(z \pm \Delta z)^2/4\sigma_z^2]$ ,  $\phi(z) = 47kz(\omega_z T)^4$ , and  $\sigma_z = 14 \mu\text{m}$  is the average size over the hold time. The center-of-mass shift due to the potential curvature is numerically found to be  $\Delta z \propto T^2 \omega_z k \sin(2n\omega_z T)$ , which is negligible compared to  $\sigma_z(t)$ . When the time-varying  $\sigma_z$  due to the compressional mode of the BEC is considered,  $\phi(z) = 4k(\omega_z T)^2 z \times [\sigma_z(4T)/\sigma_z(0) - 1]$ , becoming effectively proportional to  $kz(\omega_z T)^3$  as the inhomogeneous dephasing for  $n = 1$  is only partially canceled out. The blue solid line in Fig. 3(a) takes this into account and shows good agreement with our experiment.

### $n=1$ and $n=2$ interferometer

Fig. 8 shows for  $n = 1$  the axial width  $\sigma_z$  and center-of-mass position (a), and the fringe contrast  $C$  and phase  $\phi$  (b). The amplitude of the phase shift calculated from the center-of-mass oscillation is  $\phi_{max} = 4ka_{max}T^2 = 0.17(1)$  rad, where  $a_{max} = \omega_z^2 z_{initial}$  and  $z_{initial} = 3.6(3) \mu\text{m}$ . The result shows good agreement with the actual interferometer phase measurement  $\phi_{max} = 0.15(2)$  rad (red points in Fig. 8(b)). The interferometer phase offset from 0 might be attributable to the asymmetry of the combined waveguide and magnetic potential.

The measured fringe contrast (blue points in Fig. 8(b)) is out-of-phase with the oscillation of the compressional mode (blue points in Fig. 8(a)) as the inhomogeneous dephasing  $\phi(z) = 4kz(\omega_z T)^2$  exacerbates the fringe contrast degradation for larger wavepacket size. The wavepacket does not perfectly overlap after the interrogation due to the potential curvature. However, the non-overlapped portion is negligible compared to the wavepacket size.

Figure 9 presents the corresponding set of data for  $n = 2$ ,  $T = 1.125$  ms,  $a_s = 1.7a_0$ . In the case of  $n = 2$ , the inhomogeneous dephasing and DC acceleration sensitivity for  $n = 1$  are canceled out by the conjugate path. We observed the modulation of fringe contrast and momentum dependent phase shift (blue diamonds in Fig. 9(c) and (d), respectively) when the pulse time interval did not compensate for the finite length of the splitting pulses (the first scheme in Fig. 9(a)). This effect can be clarified by solving the Schrödinger equation,

$$i \frac{d\psi}{dt} = \left[ \frac{\hbar}{2m} \frac{d^2}{dz^2} + \Omega(t) \cos(2k_0 z + \theta/2) \right] \psi, \quad (3)$$

where  $\Omega(t)$  and  $k_0$  are the time-dependent light shift potential and the light wavevector, respectively. Expanding the wave function in the Bloch basis and substituting it in Eq. (3) gives

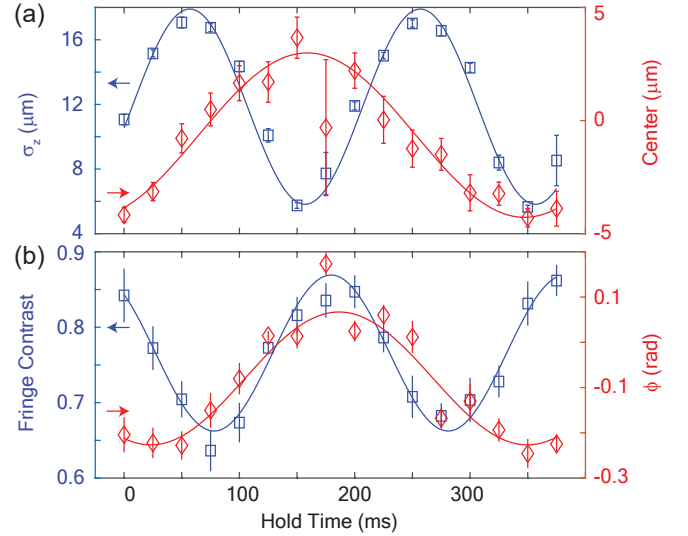


FIG. 8.  $n = 1$  interferometer. (a)  $\sigma_z$  (left) and center-of-mass position (right), and (b) fringe contrast (left) and phase (right) are presented as a function of hold time for  $T = 2.125$  ms,  $a_s = 1.7a_0$ . Solid lines are sinusoidal fits. The oscillations in  $\sigma_z$  and fringe contrast (center and  $\phi$ ) are out-of (in)-phase, with a small shift due to the time-of-flight. Error bars are  $1\sigma$ .

$$i \frac{dC_{2j}(k, t)}{dt} = \frac{\hbar}{2m} (2jk_0 + k)^2 C_{2j}(k, t) + \frac{\Omega(t)}{2} \left[ C_{2j-2}(k, t) e^{i\theta/2} + C_{2j+2}(k, t) e^{-i\theta/2} \right]. \quad (4)$$

After taking the initial condition to be atoms at rest and assuming a perturbative regime in which  $C_{2j}(k, 0) = \delta_{j,0}f(k)$

and  $\Omega(t) \ll 32\omega_r$ , where  $|f(k)|^2$  is a narrow ( $\Delta k \ll k_0$ ) momentum distribution centered at 0 and  $\omega_r = \hbar k_0^2/2m$ , Eq. (4) is truncated to the lowest 3 states,

$$\begin{aligned} i\dot{C}_0 &= \frac{\Omega(t)}{2}(C_{-2} + C_2) \cos \frac{\theta}{2} + i\frac{\Omega(t)}{2}(C_{-2} + C_2) \sin \frac{\theta}{2}, \\ i\dot{C}_2 &= 4\omega_r \left(1 + \frac{k}{k_0}\right) C_2 + \frac{\Omega(t)}{2} e^{i\theta/2} C_0, \\ i\dot{C}_{-2} &= 4\omega_r \left(1 - \frac{k}{k_0}\right) C_{-2} + \frac{\Omega(t)}{2} e^{-i\theta/2} C_0. \end{aligned} \quad (5)$$

Note that the kinetic energy associated with  $k$  has been subtracted by a unitary transformation. Eq. (5) is numerically solved with an appropriate potential shape  $\Omega(t)$  as in Fig. 9(a). IN Eq. (5)  $\theta$  is the relative phase between the recombination and the splitting pulses, so  $\theta$  is set to 0 for all the pulses except the recombination pulse. The initial center-of-mass momentum  $k$  in Eq. (5) can cause a phase shift between the left and right atoms at the time of recombination. This happens when the amount of time the atoms spent in the bases  $C_{-2}$  and  $C_2$  are not equal. The timing compensation  $\delta T = 22 \mu\text{s}$  determined numerically was found experimentally to optimize the fringe contrast and to flatten the momentum-dependent phase shift as in Fig 9(c) and (d). Note that the compensation is valid until  $\hbar k < 0.05\hbar k_0$ , which is much larger than the initial momentum of our BEC ( $< 0.01\hbar k_0$ ) induced by the loading process.

### Scaling behavior of cold collisions

The multiple-loop atom interferometer suffers from cold collision-induced atom loss [21] that can usually be neglected for a small number of loops. As shown in Fig. 1(a), the atomic wave packets pass through each other once for every mirror pulse, and so the chance of a collision scattering an atom out of the coherent wave packet is  $n$  times larger than the  $n = 1$  single reflection scheme. It results in a collisional loss that scales as  $dN_{tot}/dn \propto -a_s^2 N_{tot}^2$ , where  $N_{tot}$ ,  $n$ , and  $a_s$  are the atom number, the number of collisions, and the s-wave scattering length, respectively. As shown in Fig. 2(b), we measured the atom number as a function of collision number for various s-wave scattering lengths. The fitted curves are the analytic solution of the differential equation  $dN_{tot}/dn = -aN_{tot}^2 - bN_{tot}$ , which is  $N_{tot}(n) = -b \exp(bc)/[a \exp(bc) - \exp(bn)]$ , where  $c$  is a constant related to the initial atom number and  $n$  is treated as a continuous variable for simplicity. The results of the least square fits are listed in Table I. From the results, the coefficient  $a$  vs.  $a_s$  is plotted in log-log scale and the scaling exponent is extracted as in Fig. 10. Note that the first two data points are not shown on the plot. We found that over the wide range

TABLE I. The results of the least square fit.

$a_s(a_0)$	$a$	$b$	$c$	$\xi^2$
1.7	$2.42(0) \times 10^{-9}$	0.0065(5)	2160(163)	8.36
14.0	$7.96(0) \times 10^{-9}$	0.0106(3)	1290(42)	4.97
26.4	$7.8(5.5) \times 10^{-7}$	0.0127(24)	1020(186)	9.11
48.8	$3.24(55) \times 10^{-6}$	0.0151(15)	811(77)	7.57
73.7	$8.19(64) \times 10^{-6}$	0.0154(13)	751(58)	5.34
102.0	$2.32(10) \times 10^{-5}$	0.0143(13)	741(62)	6.10
150.4	$3.11(24) \times 10^{-5}$	0.0161(23)	640(88)	14.6

$a_s = -2 \sim 150a_0$  fringe contrast remained flat with  $C > 0.7$ ) regardless of  $n$ , as long as atom numbers were well above the detection noise. That result suggests that dephasing from the interatomic interaction is negligible compared to the collisional loss for our interrogation time-scales and atomic density. Note that the initial mean atomic density at  $a_s = 1.7a_0$  is estimated as  $2.9\text{E}13 - 4.5\text{E}13 / \text{cm}^3$ , depending on the initial loading condition.

The mirror pulse efficiency  $1 - b$  has the highest value at  $a_s < 6a_0$ , and gradually reduces at larger  $a_s$  because of the enlarged interaction-induced momentum width [15, 22, 23]. Note that the initial center-of-mass momentum also degrades the mirror efficiency but the theoretical upper bound for our case is 99.98%, which is negligible degradation. However, the momentum width from the compressional mode currently limits the mirror efficiency to 99.4%. An atom number  $N_{tot} \sim 800$  remains after  $n = 400$  reflections with the current mirror efficiency, which is comparable to the atom and photon shot noise of 150 atoms.

### Quantum lock-in amplification of atom interferometer

The multiple-round trip scheme allows for phase-synchronous measurement of a suitably-modulated perturbation, a realization of quantum lock-in amplification [18]. To make a proof-of-principle demonstration of this capability, the waveguide intensity was modulated as  $I(t) = I_0[1 + A \times \sin(2\pi F \times t + \varphi)]$ . Note that since the initial atom position is displaced from the waveguide waist position, the

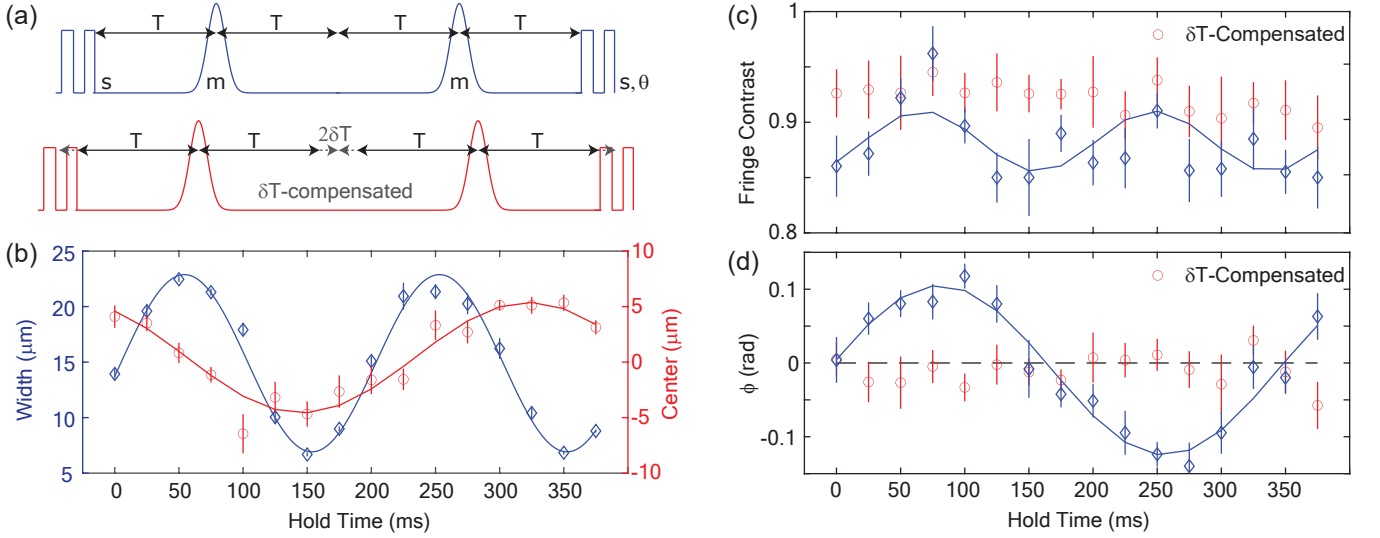


FIG. 9.  $n = 2$  interferometer. (a) The pulse timing that compensates the finite splitting pulse length (bottom), compared to a careless timing (top). (b) The axial width  $\sigma_z$  and center-of-mass position as a function of hold time. The fringe contrast (c) and the phase (d) for  $n = 2$ ,  $T = 1.125$  ms,  $a_s = 1.7a_0$ . The splitting pulse compensation (red circles) and the other (blue diamonds) are compared. Error bars are  $1\sigma$ . The fringe contrast is modulated in-phase to the axial width, and the interferometer phase is modulated  $90^\circ$  in advance to the center-of-mass.

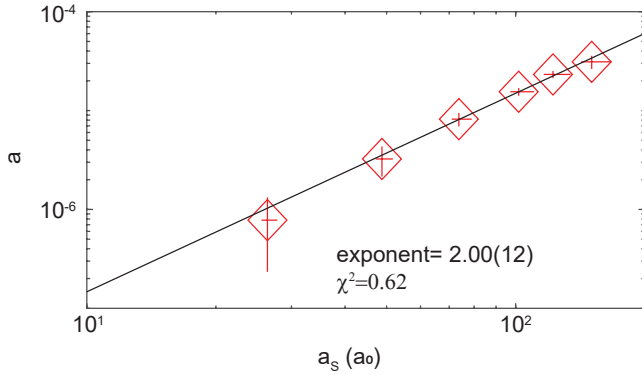


FIG. 10. The coefficient  $a$  as a function of  $a_s$  in log-log plot. The black solid line is the least-square fit, extracting the scaling exponent. Error bars are  $1\sigma$ . The s-wave scattering length is  $a_s = -29a_0 \times [1 + 56 \text{ G}/(B - 562.2 \text{ G})]$ , and the  $B$  field is independently measured by RF spectroscopy of the atoms.

waveguide beam intensity modulation induces a modulated acceleration  $a(t) = a_{max} \times A \times \sin(2\pi F \times t + \varphi)$ . The laser phase is  $\phi_{laser} = 8k_0 \sum_{j=1}^{j=n} (-1)^j a_{max} A / (2\pi F)^2 =$

$32k_0 a_{max} T^2 n / \pi^2$  for  $F = 1/(4T)$ , and  $\varphi = 0$ . From the data of Fig. 11(b), we estimated  $a_{max} = 4.85(15) \times 10^{-5} \text{ m/s}^2$ . Note that the odd-parity operation of successive shots of alternating  $\varphi = \{0, \pi\}$  (i.e. differential average) mitigates the systematic phase shift. We estimate the beam waist displacement  $z$  that satisfies  $a_{max} = -dU(z)/(mdz)$ , where  $U(z) = U_0 w_0 / [1 + (z/z_R)^2]$ ,  $U_0 = 4.6 \text{ } \mu\text{K}$ ,  $w_0 = 100 \text{ } \mu\text{m}$ , and  $z_R = \pi w_0^2 / 1064 \text{ nm}$ . The beam waist location is estimated as 4.5 mm away from the atom position, which is smaller than the Rayleigh length 30 mm.

Figure 11(c) shows the Allan deviations of the raw phase and the odd-parity phase, respectively. The odd-parity operation improves long-term stability as the systematic phases were canceled out. The black dotted line consists of 30% atom and photon shot noise, and 70% mirror vibration and laser phase noise.

Figure 11(d) and (e) present the response of lock-in amplification as a function of  $\varphi$  and  $F$ , respectively. The theory curves are from Eq. (1). The theoretical gain of the lock-in amplifier is  $\log_{10}(n/2)$  dB. When the system is atom shot-noise limited, it has maximum SNR at  $n = \sqrt{1/b}$ .



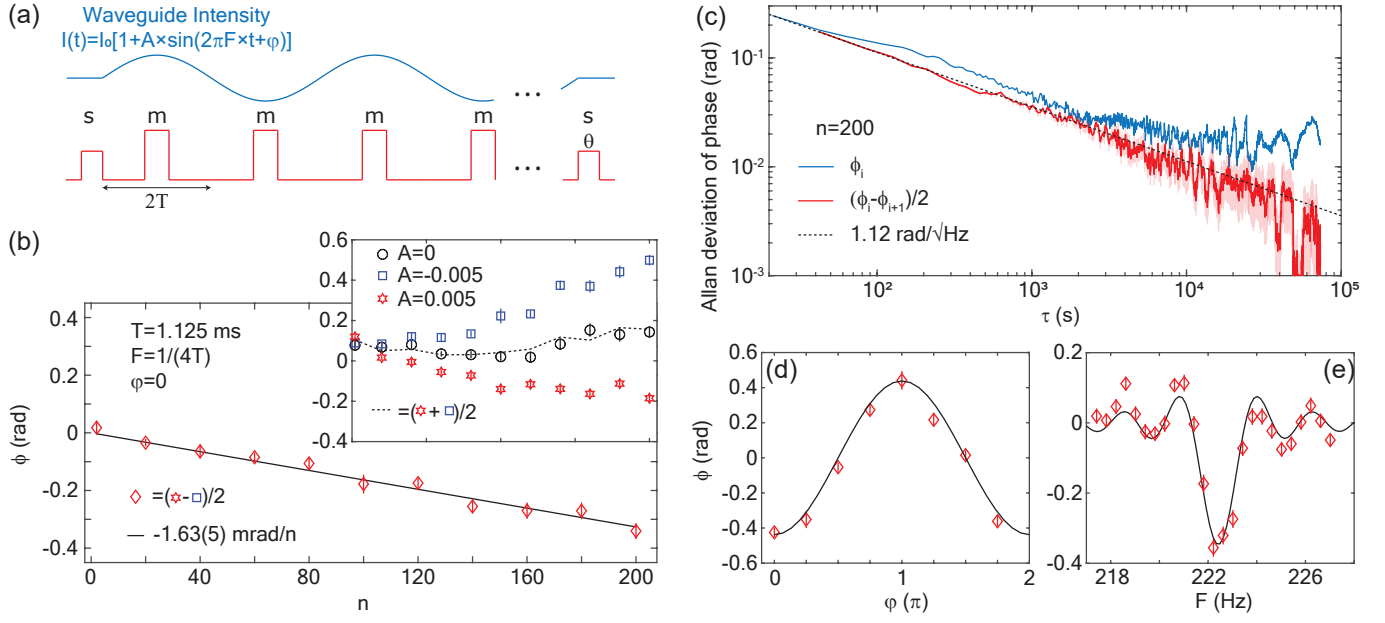


FIG. 11. Quantum lock-in amplification of the atom interferometer. (a) The scheme for phase-synchronous signal measurement. The intensity of the waveguide is modulated. (b) Linear amplification of the interferometer phase  $\phi$  as a function of  $n$  for a modulated waveguide intensity. Symbols are odd-parity phases. The line is a linear fit. Up to 20 dB signal amplification is demonstrated. (inset) Symbols are  $\phi$  vs.  $n$  for different modulation amplitudes. The black dotted line is even-parity phase that corresponds to systematic phase shift at  $A = 0$ . (c) Allan deviation of  $\phi$  for raw data (blue) and odd-parity of successive phases (red) for  $n = 200$ . The odd-parity operation reduces systematic shift and long-term drift. (d)  $\phi$  (symbols) as a function of  $\phi$  for fixed  $A$  and  $F = 1/(4T)$ . The black line is a sine curve fit. The presented  $\phi$  is offset by the systematic phase. (e) Odd-parity phases (symbols) vs.  $F$  and  $A = 0.005$ . The black line is from lock-in amplifier theory.  $\phi$  is measured by either scanning  $\theta$  [(b),(d)] or fixing  $\theta$  at the steepest slope [(c),(e)]. Error bars are the standard error in the mean.